Urban Surface Reconstruction in SAR Tomography by Graph-Cuts

Clément Rambour, Loïc Denis, Florence Tupin, Hélène Oriot, Yue Huang, Laurent Ferro-Famil

Urban Surface Reconstruction in SAR Tomography by Graph-Cuts

Clément Rambour, Yué Huang, Clement Rambour, Loïc Denis, Florence Tupin, Hélène Oriot, Yue Huang, Laurent Ferro-Famil

Urban Surface Reconstruction in SAR Tomography by Graph-Cuts

Clément Rambour[a,*], Loïc Denis[b], Florence Tupin[a], Hélène Oriot[c], Yue Huang[d], Laurent Ferro-Famil[d],

[a] *LTCI, Télécom ParisTech, Université Paris-Saclay, 75013 Paris, France*
[b] *Univ Lyon, UJM-Saint-Etienne, CNRS, Institut d Optique Graduate School, Laboratoire Hubert Curien UMR 5516, F-42023, SAINT-ETIENNE, France*
[c] *ONERA, The French Aerospace Laboratory, 91761 Palaiseau, France*
[d] *Institute of Electronics and Telecommunications of Rennes (IETR), University of Rennes 1, Rennes, France*

ABSTRACT

SAR (Synthetic Aperture Radar) tomography reconstructs 3-D volumes from stacks of SAR images. High resolution satellites such as TerraSAR-X provide images that can be combined to produce 3-D models. In urban areas, sparsity priors are generally enforced during the tomographic inversion process in order to retrieve the location of scatterers seen within a given radar resolution cell. However, such priors often miss parts of the urban surfaces. Those missing parts are typically regions of flat areas such as ground or rooftops. This paper introduces a surface segmentation algorithm based on the computation of the optimal cut in a flow n etwork. This segmentation process can be included within the 3-D reconstruction framework in order to improve the recovery of urban surfaces. Illustrations on a TerraSAR-X tomographic dataset demonstrate the potential of the approach to produce a 3-D model of urban surfaces such as ground, façades and rooftops.

1. Introduction

SAR tomography is a remote sensing technique that can retrieve 3-D representations of diffuse environments such as forested or ice areas (Reigber and Moreira, 2000). Under the assumption that those media are mostly homogeneous, the covariance matrix at each radar resolution cell can satisfactorily be estimated by local averaging. Efficient spectral analysis techniques can then be used to invert these covariance matrices and identify the height distribution of the radar reflectivity.

With the improvement of the available spatial resolution and the large time-series, SAR tomography is also being used to analyze complex environments such as urban areas. Well-established estimators from the spectral analysis theory such as Capon beamforming (Capon, 1969) (P. Stoica, 1997), MUSIC (Schmidt, 1986), Weighted Subspace Fitting (WSF) (Viberg et al., 1991) or the more recent SPICE (Stoica et al., 2011) can be used to retrieve

*Corresponding author:
e-mail: clement.rambour@telecom-paristech.fr (Clément Rambour)

the 3-D distribution of the backscattering targets from the radar covariance matrices. However, estimating the covariance matrices is very difficult in dense urban configurations due to the spatial heterogeneity. Spatial averaging leads to blurring phenomena that bias the 3-D inversions. Considering compressed sensing techniques, the well-known approaches such as in (Zhu and Bamler, 2010; Budillon et al., 2011) are based on ℓ_1-norm minimization in the single-snapshot case, so they do not require to estimate the data covariance matrix. They nonetheless achieve super-resolved estimation of the scatterers heights. A recent extension of the conventional single look Compressed Sensing (CS) has been proposed (Rambour et al., 2018) in order to also consider the 3-D relationship between scatterers through spatial regularizations.

With spaceborne sensors, these techniques can be used to obtain a 3-D representation of vast areas on the ground. Those 3-D models have numerous applications such as town planning, city management or crisis monitoring. However, because of the large contrasts between back-scattered powers in urban areas (ground level and roof tops return much weaker echoes than structures on façades), the obtained 3-D models are accurate on some building walls but suffer from holes or large errors elsewhere.

Different techniques exist to recover the geometrical shapes of urban areas from tomographic reconstructions. The proposed approaches generally use discretized representations of the reconstructed volume to find a surface that represents best the observed scene. Works (Zhu and Shahzad, 2014) and (Shahzad and Zhu, 2016) propose to extract building shapes using numerous image processing techniques on the obtained point cloud (region growing, directional filtering, clustering, polygon fitting). In (Ley et al., 2018), Ley *et al.* propose to minimize the Total Variation (TV) of the height map that best fits the observed points. They introduce the idea that along a given ray incoming from the sensor, only a single scatterer is expected to be recovered. This hypothesis is particularly well-suited to urban areas where surfaces scatter most of the incoming wave so that down-stream surfaces are occluded (in the shadow). The observed scene can then be described as a piecewise smooth surface. When minimizing the TV of the estimated height map, holes in the structures are filled thanks to the spatial regularization constraint (by constant height areas).

Given the numerous successes of learning-based techniques in computer vision, one may wonder whether such techniques could be applied to the problem of reconstructing urban surfaces from tomographic SAR stacks. SAR tomography consists of retrieving a 3-D image from a stack of 2-D measurements. It is fundamentally an inverse problem since it involves unmixing the signals from several scatterers that project within the same SAR resolution cell. It is important to include geometrical information that relates pixels in the 3-D reconstruction to resolution cells in the 2-D SAR images and to account for the delays (i.e., phase shifts) due to the acquisition geometry. Imposing geometrical priors to improve the 3-D reconstruction could be done using learned priors or a deep neural network, however, a strong interaction between the geometrical modeling corresponding to the forward model and the spatial regularization is needed. If only a segmentation approach is considered, starting from a given tomographic reconstruction, a difficulty arises from the reconstruction artifacts (sidelobes) that are very specific to the acquisition geometry and that might require retraining a learning-based segmentation technique for each tomographic stack to efficiently remove these specific artifacts. Given the difficulty in producing tomographic

SAR stacks and associated 3D ground truths, or of simulating realistic SAR stacks from a 3D model (with the temporal and geometrical decorrelation effects), learning-based models do not seem to be, to date, a viable option.

In this paper, we describe the urban scene as piecewise smooth surfaces and seek a segmentation of the urban surfaces as an optimal cut in a particular graph. To better express geometrical regularity properties, we segment the scene in ground geometry. The so-called ground geometry is composed of two axes that define the horizontal plane and the vertical direction *cf.* Fig. 2. We also use the estimated 3-D reflectivity as input for the surface segmentation instead of providing a list of extracted 3-D points. As the proposed segmentation algorithm is very generic, any SAR tomographic algorithm can be used as input.

Given the superior results obtained when combining the 3-D inversion algorithm (Rambour et al., 2018) with the surface segmentation, we propose to combine them both by alternating a step of reflectivity estimation with a step of surface segmentation. We call this algorithm REDRESS for Alte**R**nat**E**d 3-**D** **RE**construction and **S**urface **S**egmentation.

The proposed contributions presented here are then a new graph-cut based segmentation algorithm to retrieve urban surface from any kind of tomographic reconstruction and an improved alternate algorithm to obtain both a 3-D estimation of the reflectivity and the urban surface. The contributions and the workflow are summarized in Fig. 1. The structure of the paper is as follows. We first describe the multi-baseline SAR signal model and state-of-the-art methods in urban SAR tomography. Then in Section 3 we introduce a graph-cut based urban surface segmentation method. In Section 4, we propose a method that combines 3-D reconstruction and surface segmentation. We illustrate the efficiency of the segmentation depending on the tomographic reconstruction algorithm used on a stack of 40 images of the city of Paris obtained by the TerraSAR-X satellite in the last section. Results obtained with the REDRESS algorithm are also presented on the same dataset.

2. State of the art in SAR tomography

2.1. Signal Model

SAR tomographic signal models are generally written at a given SAR resolution cell. However, to be able to express a spatial regularization, we prefer to define the reflectivity distribution in the 3-D space. A SAR tomographic stack is obtained from N Single Look Complex (SLC) SAR images by spatial co-registration on a master image. The geometry of the scene is depicted in Fig. 2. The complex amplitude at a given resolution cell of the images can be modeled as the sum of the back-scattered amplitudes produced by all scatterers that are seen within that same radar resolution cell. For the n-th image, the complex amplitude of the pixel at the azimuth-range position (x', r') is:

$$\underline{v}_n(x', r') = \iiint \underline{f}(x' - x, r' - \rho_{n;y,z})\underline{u}(x, y, z) \cdot \exp\left(-\frac{4\underline{j}\pi}{\lambda}\rho_{n;y,z} + \underline{j}\varphi_{\text{atmo}}\right)\mathrm{d}x\,\mathrm{d}y\,\mathrm{d}z + \underline{\epsilon}(x', r') \quad (1)$$

where complex-valued variables are underlined for clarity, the variables x, y and z denote the coordinates in the ground geometry whereas x' and r' correspond to the coordinates along the azimuth and range axes. The distance $\rho_{n;y,z}$ is the distance of a scatterer at location (x, y, z) to the closest point of the n^{th} sensor trajectory, and

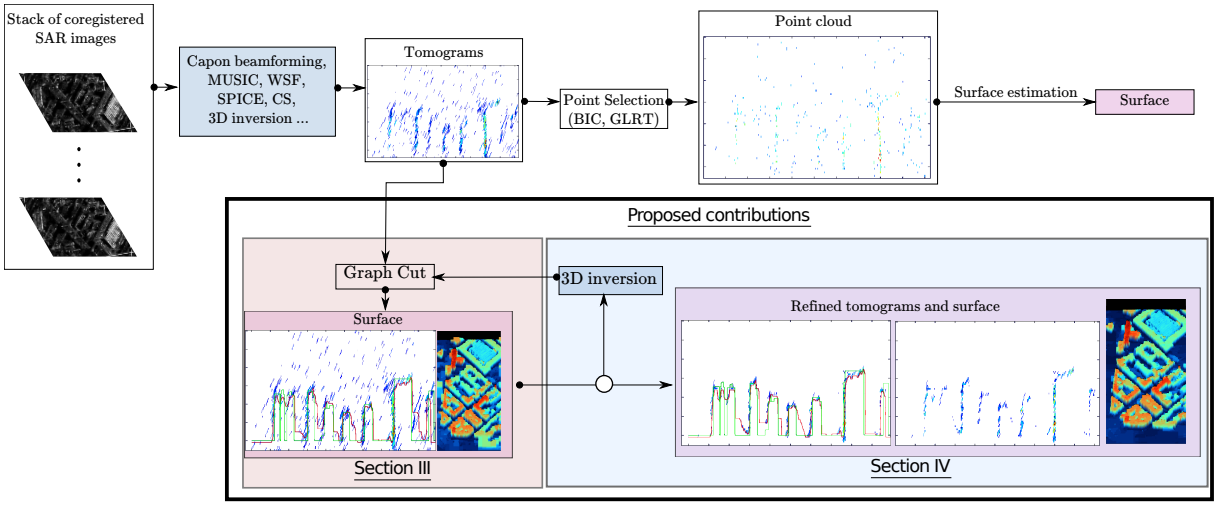

Fig. 1. Overview of the article and proposed workflow. Starting from a stack of coregistered SAR images, different SAR tomographic techniques can be used to retrieve a 3-D estimation of the reflectivity. As the reconstructions are generally corrupted with noise and/or outliers, urban surface segmentation algorithms are generally applied on a point cloud extracted from the tomograms. The number of points is obtained either by minimizing an information criterion such as BIC or AIC or through hierarchical hypothesis testing. Rather than extracting a set of points, we estimate directly the urban surface on the tomograms by a graph-cut method (see section 3). We also derive an alternating scheme that iteratively estimates the urban surface and uses it to improve the tomographic inversion (see section 4).

$\underline{f}$ represents the Point Spread Function (PSF). φ_{atmo} is the phase noise due to the atmospheric phase screen. The random variable $\epsilon(x', r')$ models the thermal noise (modeled as a white additive Gaussian process).

Each image is acquired from a slightly different angle at each pass of the sensor. This angular diversity induces a different distance $\rho_{n;y,z}$ to each antenna. Upon proper sampling, co-registration and spectral apodization to reduce sidelobes, the PSF can be roughly approximated by a 2-D Dirac, leading to the following simplification:

$$\underline{v}_n(x', r') = \iint_{(y,z)\in\Delta_{r'}} \underline{u}(x', y, z).\exp\left(-\frac{4\underline{j}\pi}{\lambda}\rho_{n;y,z} + \underline{j}\varphi_{\text{atmo}}\right) \mathrm{d}y\,\mathrm{d}z + \underline{\epsilon}(x', r')\,, \tag{2}$$

where the integration is carried out over points $(y, z) \in \Delta_{r'}$, i.e., points such that $\rho_{n;y,z} = r'$. The tomographic stack can be pre-processed as a multi-baseline interferometric stack in order to directly relate the phases to heights. Under some classical approximations (see (Fornaro et al., 2003) for details), and after removal of the atmospheric phase screen, (2) can be written:

$$\underline{v}_n(x', r') = \iint_{(y,z)\in\Delta_{r'}} \underline{u}(x', y, z) \exp\left(-\underline{j}\underline{\xi}_n z\right) \mathrm{d}y\,\mathrm{d}z + \underline{\epsilon}\,. \tag{3}$$

The r'-th radar resolution cell is defined by:

$\Delta_{r'} = \{\ (y, z)\ |\ r' - \delta_{\text{range}}/2 \leq \rho_{y,z} \leq r' + \delta_{\text{range}}/2\ \}$, with δ_{range} the step in range direction. The set Δ_r is thus the extension of the radar resolution cell along its elevation direction h (*cf. Fig. 2*). The parameter $\underline{\xi}_n = \frac{4\pi b_n}{\lambda r' \sin\theta}$ is the spatial impulse associated to the sampling of the scene for each baseline, b_n is the n-th baseline, θ the incidence angle of the master sensor and λ the radar wavelength.

2.2. Covariance based techniques

In most of SAR tomographic approaches, the inversion is performed resolution-cell by resolution-cell, keeping the original radar geometry. A 3-D representation of the scene is then obtained by merging all 1-D inversions.

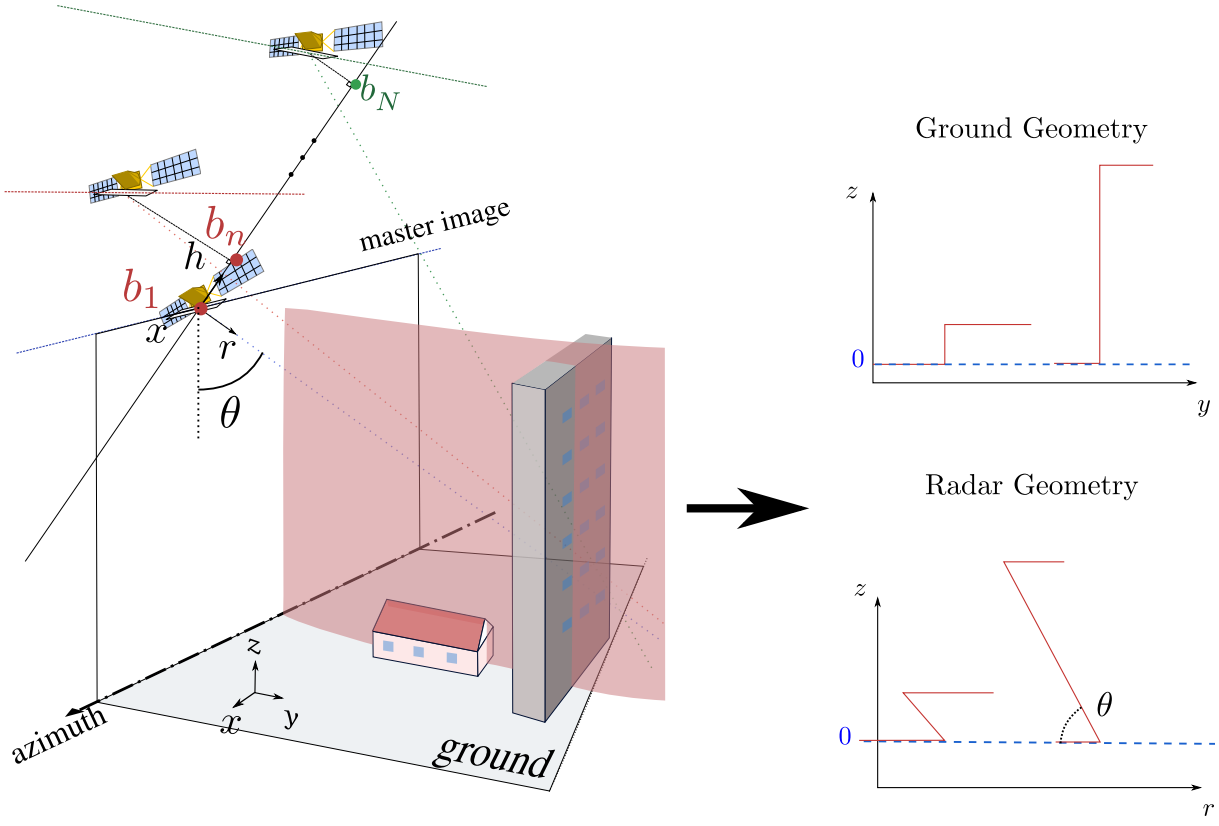

Fig. 2. Geometry of the 3-D scene. Two geometric configurations can be used to describe the scene: the ground geometry associated with the coordinate system (x, y, z) and the radar geometry associated with the coordinate system (x, r, z). On the left hand side, the different coordinates system are illustrated on a simple urban scene model. On the right hand side, a sketch of a tomographic profile corresponding to the red slice in each geometry.

Throughout this section, we will consider the complex amplitudes measured at given pixel. We denote by $\underline{\boldsymbol{y}} \in \mathbb{C}^N$ the vector formed by the complex amplitudes observed at the pixel of interest on each of the N images. This signal results from the back-scattering produced by scatterers with reflectivity $\underline{\boldsymbol{u}} \in \mathbb{C}^D$, each scatterer located at the same range but at D different elevations along the z axis. By discretization of equation (3), the model of the measurement corresponds to the following linear model under additive noise:

$$\underline{\boldsymbol{y}} = \underline{\boldsymbol{A}}(z) \cdot \underline{\boldsymbol{u}} + \underline{\boldsymbol{\epsilon}} \tag{4}$$

where matrix $\underline{\boldsymbol{A}}(z) \in \mathbb{C}^{N \times D}$ is called the sensing or steering matrix and consists of the concatenation of the D steering vectors associated to each scatterer of the radar cell. It depends on the sampling of elevations $\boldsymbol{h}$. A steering vector $\underline{\boldsymbol{a}}_{1 \leq k \leq D} \in \mathbb{C}^N$ is defined by

$$\underline{\boldsymbol{a}}_k = \left[\exp(-j\underline{\xi}_1 z_k) \cdots \exp(-j\underline{\xi}_N z_k)\right]^{\mathrm{t}} \tag{5}$$

Many estimators exist in the field of spectral analysis to invert (4). They all require an estimate of the covariance matrix $\underline{\boldsymbol{R}} = \mathbb{E}[\underline{\boldsymbol{a}}_k \underline{\boldsymbol{a}}_k^{\mathrm{H}}] \in \mathbb{C}^{N \times N}$ at the pixel of interest. As discussed in the introduction, estimating this covariance matrix by local averaging is tricky in heterogeneous regions (high risk of mixing signals corresponding to very

different scatterers configurations) and when considering large stacks (the sample covariance matrix is singular unless a least N samples are averaged, which might represent more than one hundred pixels).

The classical beamforming and the Capon beamforming are two popular nonparametric estimators that lead to good results in the SAR tomographic representation of continuous reflectivity profiles such as in forests or ice. Due to their simplicity and computational efficiency, they can provide a quick overview of urban landscape. However, as classical beamforming does not provide a side-lobe suppression, outliers are likely to occur on urban areas where dynamic range is much larger than it is in forests or ice regions. Several methods consider a limited number of scatterers $D < N$ (sparse spectral estimators): MUSIC (Schmidt, 1986) and the related WSF techniques (Viberg et al., 1991; Huang et al., 2010). MUSIC is built on the consideration that, when there are $D < N$ scatterers located at D given locations, the observed vector of complex amplitudes is located close to the sub-space spanned by the corresponding D steering vectors. Hence, the $N - D$ lowest eigenvalues of the covariance matrix span the complementary orthogonal sub-space (the so-called noise subspace). In WSF this idea is refined by including the distribution of the noise eigenvectors of the empirical covariance matrix. When only the noise subspace is considered this approach is called NSF for Noise Subspace Fitting. Beside an estimation of the covariance matrix, those techniques also require an estimation of the number of scatterers present in each radar cell.

The recent SPICE method (Stoica et al., 2011) is a fully non-parametric sparse algorithm based on the minimization of a covariance fitting criterion between the estimated covariance matrix and its theoretical expression according to (4). This algorithm achieves a very good performance when the covariance matrix is correctly estimated and when the discrete model is respected.

2.3. Regularized inversion

More suited to dense urban areas than methods based on covariance matrix analysis, CS has proved to be able to achieve super-resolution in the scatterers unmixing (Zhu and Bamler, 2010; Budillon et al., 2011). Since no covariance matrix estimation is required, this method avoids the resolution-loss implied by filtering-based covariance estimation. CS performs the inversion of (4) under a sparse prior:

$$\underline{\hat{\boldsymbol{u}}} = \underset{\underline{\boldsymbol{u}}}{\operatorname{argmin}} \ \|\underline{\underline{\boldsymbol{P}}}\,\underline{\boldsymbol{u}} - \underline{\boldsymbol{v}}\|_2^2 + \mu\|\underline{\boldsymbol{u}}\|_1 \tag{6}$$

The parameter μ balances the importance of the sparsity prior with respect to the data fidelity. $\underline{\underline{\boldsymbol{P}}}$ is a block diagonal matrix with each block being the steering matrix $\underline{\boldsymbol{A}}$ associated to the pixels in the SAR images.

In urban areas where bright scatterers can be located near empty radar cells this parameter tuning can be challenging (i.e., require *local* tuning). Although being parametric, parameter μ is not directly expressed in terms of the number of scatterers in the cell.

Instead of performing the inversion in the radar geometry, the 3-D inversion (Rambour et al., 2018) is performed directly in ground geometry to allow the use of geometrical priors. However if only a sparse prior is used we obtain the equivalent problem:

$$\underline{\hat{\boldsymbol{u}}} = \underset{\underline{\boldsymbol{u}}}{\operatorname{argmin}} \|\underline{\underline{\boldsymbol{\Phi}}}\,\underline{\boldsymbol{u}} - \underline{\boldsymbol{v}}\|_2^2 + \mu\|\underline{\boldsymbol{u}}\|_1 \tag{7}$$

where the linear operator $\underline{\mathbf{\Phi}}$ maps the complex-valued reflectivities of the scatterers sampled in ground geometry to the measurements (complex amplitudes on the SAR antennas):

$$\underline{\mathbf{\Phi}}_{k,\ell} = \begin{cases} 0 & \text{if } \rho_{1;y_\ell,z_\ell} \notin [r'_k - \frac{\delta_{\text{range}}}{2}, r'_k + \frac{\delta_{\text{range}}}{2}] \\ \exp(-\underline{j}\varphi_\ell) & \text{otherwise,} \end{cases} \tag{8}$$

with φ_ℓ the phase model given either by equation (1): $\varphi_\ell = 4\pi\rho_{n;y_\ell,z_\ell}/\lambda$, or by equation (2): $\varphi_\ell = \xi_n z_\ell$.

Equations (6) and (7) differ only from their inverse operator and thus in the final geometry in which $\underline{\boldsymbol{u}}$ is described. We chose the second framework to perform the sparse inversion as it can be more easily extended to locally adapt the weight of the sparsity prior according to the urban surface retrieved by the graph-cut segmentation technique described next.

3. Graph-cut based surface segmentation

Starting from the tomographic reconstruction obtained with one of the methods described in the previous section (a 3-D volume $u(x, y, z)$), we aim to recover the urban surfaces (ground, building facades, roofs). Following a typical approach in computer vision for surface reconstruction, we formulate the problem as an energy minimization problem. We seek a surface $\mathscr{S}$ corresponding to an elevation map: $(x, y) \mapsto z = \mathscr{E}(x, y)$ that both fits well the reconstructed tomographic volume and that is smooth. We first formulate a cost function that captures these two properties, then we describe an efficient graph-based algorithm to perform the minimization of the cost function.

3.1. Definition of the cost function

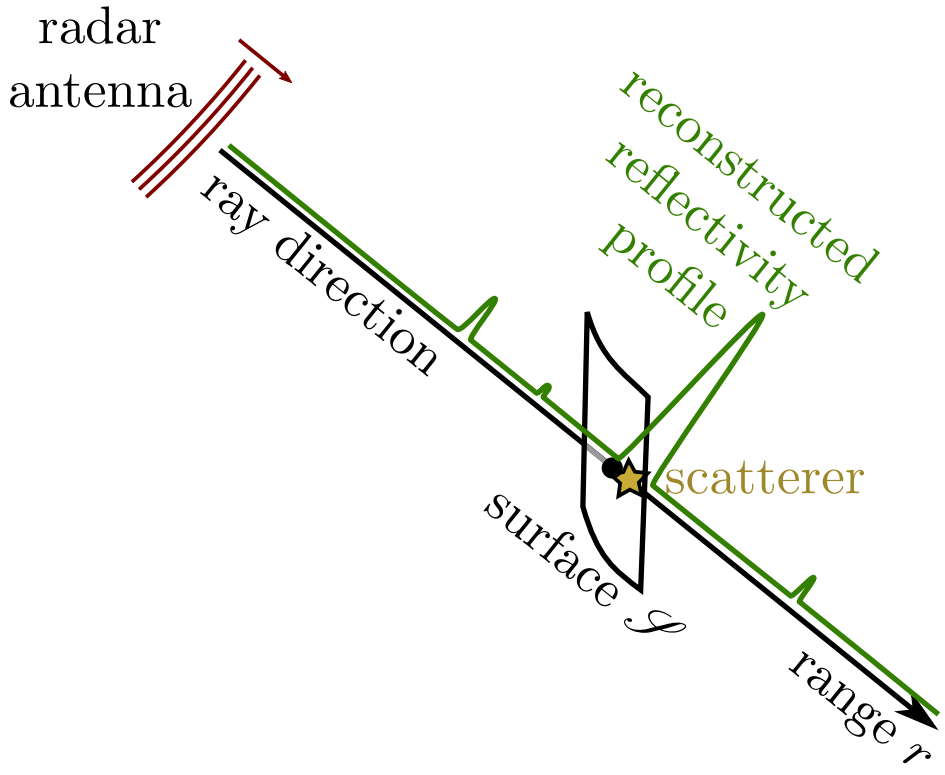

Fig. 3. We seek a surface $\mathscr{S}$ that, for each ray, is close the scatterer(s) found along the ray.

The first component of the cost function favors surfaces that are faithful to the reconstructed tomographic volume. We seek surfaces such that, when considering a given ray direction in 3-D space, the scatterer encountered along the ray falls close to the ray-surface intersection, see Fig.3. The reflectivity profile along the ray may display several local maxima due to residual sidelobes after the tomographic inversion. Rather than detecting these maxima and deciding for the most meaningful maximum, we consider that a satisfying location of the surface is a location such that the reflectivity profile is split into two well-balanced halves. We define the cumulative reflectivity $C^-(r_s)$ from the antenna to the surface $\mathscr{S}$ and the cumulative reflectivity $C^+(r_s)$ from the surface to the maximum range:

$$C^-(r_s) = \int_{r_{\min}}^{r_s} |u(r)| \, \mathrm{d}r, \tag{9}$$

$$C^+(r_s) = \int_{r_s}^{r_{\max}} |u(r)| \, \mathrm{d}r \,, \tag{10}$$

where r_s is the range of the surface, i.e., the distance from the radar to the surface, in the direction of the ray. If the surface is such that $C^-(r_s) < C^+(r_s)$, then it is too close to the radar: most of the reflectivity of the scatterers encountered along the ray is located beyond the surface. Conversely, if $C^-(r_s) > C^+(r_s)$, the surface is too far from the radar: scatterers accounting for most of the reflectivity are located before the surface. The imbalance $C^-(r_s) - C^+(r_s)$ is therefore an indication of bad surface localization. In order to favor surfaces that are located close to the position of equilibrium, we define the penalty:

$$D(r) = \int_{r_{\min}}^{r} \left[C^-(r_s) - C^+(r_s)\right]_+ \mathrm{d}r_s + \int_{r}^{r_{\max}} \left[C^+(r_s) - C^-(r_s)\right]_+ \mathrm{d}r_s \,, \tag{11}$$

where the notation $[\cdot]_+$ denotes the positive part: $\forall w$, $[w]_+ = \max(w, 0)$. The term $\left[C^-(r_s) - C^+(r_s)\right]_+$ in the first integral of equation (11) is non-zero only if the distance r_s is larger than the distance of equilibrium r_{equi} (where r_{equi} is such that $C^+(r_{\text{equi}}) = C^-(r_{\text{equi}})$). Then, if $r > r_{\text{equi}}$, the first integral equals $\int_{r_{\text{equi}}}^{r} \left(C^-(r_s) - C^+(r_s)\right) \mathrm{d}r_s$. Conversely, the second integral in (11) is non-zero only if the distance r_s is smaller than the distance of equilibrium r_{equi}. It is then equal to $\int_{r}^{r_{\text{equi}}} \left(C^+(r_s) - C^-(r_s)\right) \mathrm{d}r_s$. $D(r)$ is thus a function that *monotonically increases with the distance* $|r - r_{\text{equi}}|$ and that is minimal and equal to zero when $r = r_{\text{equi}}$.

The second component of the cost function guarantees that the segmented surface is smooth. To prevent the surface from oscillating in order to pass through the position of equilibrium r_{equi} for each ray, we penalize the area $\mathscr{A}(\mathscr{S})$ of the surface. In order to favor surfaces with horizontal or vertical parts, we suggest measuring the area with respect to the ℓ_1 distance (i.e., Manhattan distance $\|\boldsymbol{p}\|_1 = |p_x| + |p_y| + |p_z|$).

To summarize, we suggest defining the segmentation as the surface $\mathscr{S}$ that is a solution to the following variational problem:

$$\min_{\mathscr{S}} \quad \int_{\text{ray} \in \mathscr{R}} D_{\text{ray}}(r_{\text{ray}\to\mathscr{S}}) \, \mathrm{d}\mathscr{R} \quad + \quad \beta \, \mathscr{A}(\mathscr{S}) \,, \tag{12}$$

where $\mathscr{S}$ is required to be representable as an elevation map $\mathscr{E}(x, y)$ (formally, there exist a function $\mathscr{E} : (x, y) \mapsto \mathscr{E}(x, y)$ such that $\mathscr{S}$ be the boundary of the epigraph of $\mathscr{E}$). To prevent from introducing too many notations, we denote 'ray' for the generic definition of a ray in an adequate parameterization (a line in 3-D space), $\mathscr{R}$ represents

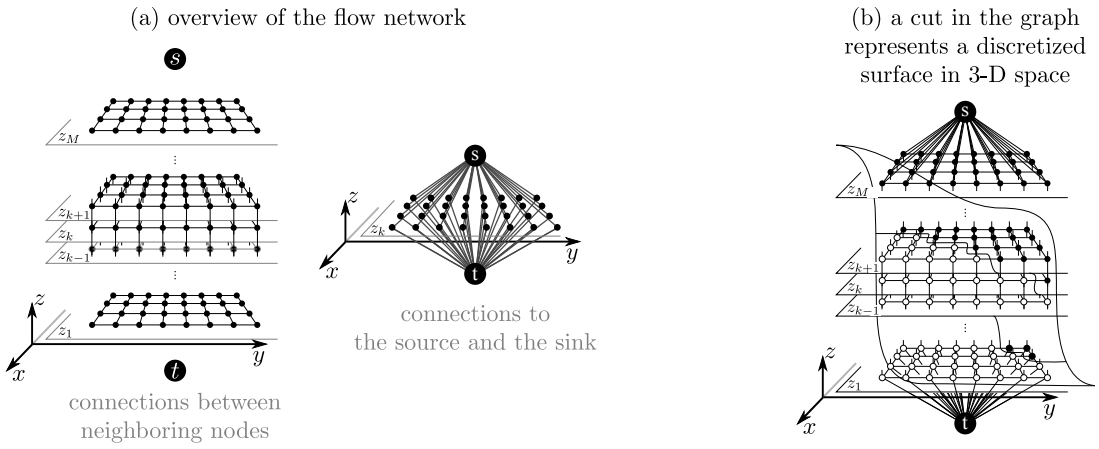

Fig. 4. Representation of the topology of the flow network: (a) a node represents a 3-D (x, y, z) location in ground geometry, each node is connected to its 6 closest neighbors and also to the source s and to the sink t; (b) a cut separates the graph into two disconnected sub-graphs, it represents a discretized version of the segmented surface $\mathscr{S}$.

the set of all rays, $r_{\text{ray}\to\mathscr{S}}$ is the distance from the radar to the surface $\mathscr{S}$ along the direction defined by 'ray', D_{ray} is the penalty defined by equation (11) for the direction specified by 'ray'. Finally, β is a parameter that balances the fidelity to the tomographic reconstruction and the spatial smoothness of the surface.

3.2. Graph-cut algorithm for minimization

The variational problem (12) is very challenging to solve. We show in this paragraph that, after discretization of the surface and of the set of rays, it can be transformed into a minimum cut problem on a particular graph. By computing the minimum cut using available efficient graph-cut libraries, we obtain a fast method to solve the surface segmentation problem.

The surface is represented by an elevation map $\mathscr{E} : \ (x, y) \mapsto z = \mathscr{E}(x, y)$ (which guarantees that it is representable as an elevation map). The horizontal location (x, y) and the elevation z are discretized. To make an easier connection between the elevation map and the surface it defines, we consider the layer cake decomposition of the elevation. With this decomposition, a discrete elevation map corresponds to a binary volume (a discrete version of the epigraph of $\mathscr{E}$) and the boundary in that volume defines the discrete surface.

We build a graph as depicted in Fig. 4, with a node to represent each voxel of the binary volume of $\mathscr{E}$. Two special nodes, called the source (denoted 's') and the sink (denoted 't') are added in order to simulate a flow from the source to the sink. Nodes are connected together by directed edges with specific capacities and a flow is said to be admissible if and only if the flow along each edge is non negative and smaller or equal to the edge capacity, and there is no flow accumulation/creation at nodes (except at the source and at the sink). By the max-flow min-cut theorem, algorithms that identify the maximum admissible flow on the graph can also identify the minimum cost cut among all possible cuts in the graph[1], see for example (Boykov and Kolmogorov, 2004). During the graph construction, by creating edges with well-chosen capacities, we can make the cost of any cut exactly match the cost of the corresponding surface in the variational formulation (12).

[1] the cost of a cut is the sum of the capacities of all edges cut that are directed from a node in the source partition to a node in the sink partition

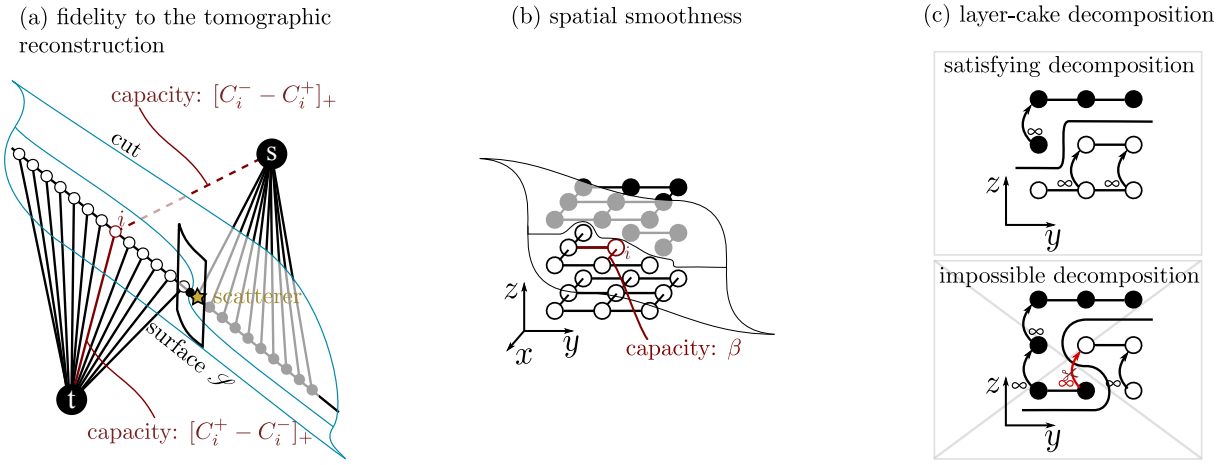

Fig. 5. The capacities of the edges are chosen so that the cost of the cut corresponds to the energy of the surface. (a) the fidelity to the tomographic reconstruction is enforced via edges originating from the source or leading to the sink. (b) the spatial smoothness of the surface is obtained by adding bi-directional edges between neighboring nodes in the x and y directions. (c) to prevent the cut from severing twice a column of nodes along the z direction, ascending edges with infinity capacity are added. These edges are counted in the total cost of the cut only when they go down-stream: from the partition containing the source to the partition containing the sink.

To represent the first term in equation (12), we substitute D_{ray} with its definition in equation (11):

$$\int_{\text{ray}\in\mathscr{R}} D_{\text{ray}}(r_{\text{ray}\to\mathscr{S}})\,\mathrm{d}\mathscr{R} = \int_{\text{ray}\in\mathscr{R}} \int_{r_{\min}}^{r_{\text{ray}\to\mathscr{S}}} \left[C^-_{\text{ray}}(r_s) - C^+_{\text{ray}}(r_s)\right]_+ \mathrm{d}r_s\,\mathrm{d}\mathscr{R} + \int_{\text{ray}\in\mathscr{R}} \int_{r_{\text{ray}\to\mathscr{S}}}^{r_{\max}} \left[C^+_{\text{ray}}(r_s) - C^-_{\text{ray}}(r_s)\right]_+ \mathrm{d}r_s\,\mathrm{d}\mathscr{R}\,. \quad (13)$$

Each of the two terms correspond to summations over a half-space whose boundary is $\mathscr{S}$: the half-space that contains the radar and the half-space with the farther ranges, respectively. We add an edge directed from the source to node i, the node that represents the 3-D position (x_i, y_i, z_i) and that is located at the distance r_i from the radar antenna. The capacity[2] of this edge is set to $\left[C_i^-(r_i) - C_i^+(r_i)\right]_+$, where C_i^- and C_i^+ are the cumulative reflectivities computed along the ray directed from the radar through the point of coordinates (x_i, y_i, z_i). Another directed edge is added from node i to the sink, with capacity $\left[C_i^+(r_i) - C_i^-(r_i)\right]_+$. To separate the graph into two parts by a cut, some edges must be severed (unless the cut passes through the distance of equilibrium r_{equi}) and the sum of the capacities of those edges corresponds to a discretization of equation (13), see Fig. 5(a).

Additional edges are created to account for the regularization term $\beta\mathscr{A}(\mathscr{S})$: bi-directional edges between pairs of nodes that are direct neighbors in the x or y directions, with capacity β, see Fig. 5(b). Finally, ascending edges with infinite capacity are included between neighboring nodes in the z direction. These edges are necessary to guarantee that the cut defines a surface that is representable by an elevation map, see 5(c). Similar edges are added in Ishikawa's graph construction that is also based on the layer-cake decomposition (Ishikawa, 2003).

In our implementation, we computed efficiently the summations along the rays by resampling the reconstructed tomographic volume in ray geometry so that sums could be carried out along columns in this new geometry. For the construction of the graph and the computation of the minimum cut, we used the graph-cuts library by Boykov and Kolmogorov (Boykov and Kolmogorov, 2004). The number of nodes in the graph is equal to the number of voxels

[2] note that an edge with zero capacity can be suppressed because it carries no flow and has no contribution to the cost of the cuts

in the estimated volume, *i.e.*, the number of pixels in one SAR image times the number of heights considered along the vertical direction. The number of edges is proportional to the number of nodes. The maximum complexity of a cut in the graph is $O(EV^2C)$ with E being the number of edges, V the number of vertices and C the value of the cut, but the experimental complexity is almost linear in the number of vertices (Boykov and Kolmogorov, 2004; Lobry et al., 2016). On a computer with an Intel(R) Xeon(R) CPU E5-2698 v4 @ 2.20GHz with 20 cores and 120 GB of RAM, finding the minimum cut takes 43 s when dealing with a volume of 8.96×10^6 voxels, for a typical value of the regularization parameter.

4. Joint reconstruction and surface segmentation

As mentioned in the introduction, the knowledge provided by the segmented urban surfaces can help to improve the inversion. The reconstruction algorithm that can most readily be extended to include segmented surfaces is the 3-D inversion method described in equation (7). Under the assumption that the signal retrieved over urban areas is mainly constituted of punctual bright points, sparsity may be an efficient enough prior to obtain clean tomograms. Nonetheless, this implies that the tuning of the sparsity parameter shall be done locally according to the position of the scatterers. In CS for SAR tomography, the sparsity constraint is generally set locally in the range and azimuth direction but constant for each radar cell. Here we propose to use the 3-D information provided by the estimated surface to go one step further and perform a spatially varying penalization of the sparsity.

When applying CS or the 3D inversion, the sparsity parameter μ is set proportional to the level of spurious elements in the reconstruction. Generally μ is set according to the noise level (Zhu and Bamler, 2012), but as decorrelation mechanisms and side-lobes should also be discarded, the knowledge of the sensor thermal noise may not be enough. Many SAR tomographic algorithms propose to estimate the number of backscattering elements in order to extract the largest scatterers in each radar cell. This step cleans the estimated tomograms from residual outliers, but is also a challenging task for large multitemporal stacks in dense environments. Moreover the CS approach may then loose one of its asset with respect to MUSIC or WSF if it also needs an estimation of the number of targets.

Under the assumption that the location of the urban surface is known, the sparsity parameter μ can be spatially tuned to lead to refined tomograms. Even when the surface is roughly known, it provides information on where the reconstructed signal should be located. In the proposed iterative algorithm, μ is computed as a function of the distance to the surface in the 3-D space and the number of iterations:

$$\mu_k(\boldsymbol{p}, \mathscr{S}) = \mu_0 + \frac{b}{(n-1)^2}\left(\frac{k}{n-k}\, d(\boldsymbol{p}, \mathscr{S})\right)^2 \tag{14}$$

where $d(\boldsymbol{p}, \mathscr{S})$ is the Euclidean distance from the point $\boldsymbol{p} = (x, y, z)^T$ to the estimated surface, k is the current iteration and n the total number of iterations. We define by $\boldsymbol{\mu}(\mathscr{S}) \in \mathbb{R}^{N_x, N_y, N_z}$ the 3-D sparsity parameter map. As the surface location estimation may be subject to errors in the first iterations, it is important to avoid over-penalizing points moderately close to the surface during the first reconstructions. This is why we multiply the distance d by a factor smaller than 1. As the number of iterations increases, the reconstruction and thus the surface estimation should be more accurate (and better in match) which suggests an increase of the penalization of the distance from

a reconstructed voxel to the surface. $\mu_0 + b$ is then the desired minimal sparsity that need to be apply to voxels not on the surface.

The proposed iterative reconstruction and surface segmentation is summarized in the REDRESS algorithm.

Algorithm Alte**R**nat**E**d 3-**D** **RE**construction and **S**urface **S**egmentation (REDRESS)

Input: $\underline{\boldsymbol{v}}$ (stack of SLC SAR images)
Output: $\underline{\hat{\boldsymbol{u}}}$ (3-D cube of complex reflectivities)
$\mathscr{S}$ (urban surface)

Initialization :
$k \leftarrow 0$
while $k < n$ **do**
  $\underline{\hat{\boldsymbol{u}}} \leftarrow$ `3-D Inversion`$(\underline{\boldsymbol{v}}, \boldsymbol{\mu}(\mathscr{S}))$
  $\mathscr{S} \leftarrow$ `graph cut`$(\underline{\hat{\boldsymbol{u}}})$
  $k \leftarrow k + 1$
end while
return $\underline{\hat{\boldsymbol{u}}}, \hat{\mathcal{S}}$

The refined tuning of the sparsity according to the surface allows to considerably improve the scatterers localization and main lobe reduction. In some cases, however, the segmented surface follows the lobe main extension direction and is not as localized as would be expected for a collection of point-like scatterers. In the global reconstruction of the scene, most of the artifacts due to the TV penalization are suppressed after 10 iterations. The obtained surface is then very close to the ground truth and provides the lowest error according to table 1.

As the 3-D inversion step estimates all the voxels at once, it can be quite computationally intensive to perform it multiple times. Using the same configuration as described previously, one iteration of this algorithm takes 2 min 49 s when estimating a 3-D scene of 8.96×10^6 voxels starting from a stack of 1.28×10^5 SAR pixels.

5. Experiments

To validate both the generality of the segmentation method and its efficiency on real data we present different experiments performed on two sets of 40 TerraSAR-X images of a part of Paris, France. The first selected area corresponds to the French Ministry of Foreign Affairs and to buildings in its neighborhood in the south west of the city. The building heights vary in a range from 10 m to 30 m. The optical view of the scenes are presented Fig. 6 and Fig. 7 side by side with the temporal average of the SAR intensities. The second scene consists in buildings next to the *rue de Grenelle*, with more diverse heights: the smallest building is only 8 m tall while the highest is close to 60 m. To evaluate our results, we built a ground truth from the building footprints and heights provided by the French geographical institute (IGN), with additional details (missing courtyard, rooftops irregularities) manually included from Google Earth™ models. Different SAR tomographic reconstruction methods introduced in section 2 (Capon Beamforming, MUSIC, WSF, SPICE, CS and the 3-D inversion) are first applied on the slice represented by the red line in Fig. 6 (b), then on the entire data sets. The segmentation by graph-cut is then performed on all the scenes. The parameter β is set to its optimal value with respect to a subset of the dataset presented in Fig. 6. The obtained surfaces are compared with the ground truth for each tomographic estimator.

(a)

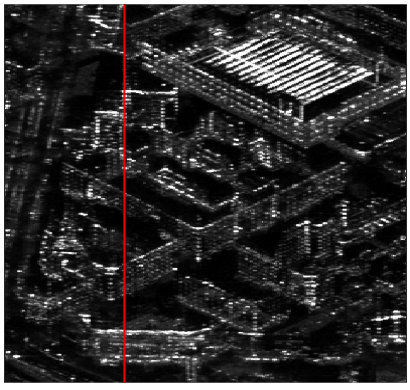

(b)

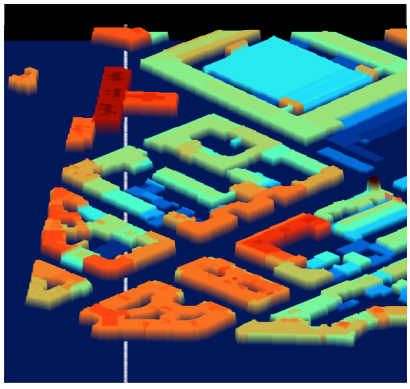

(c)

Fig. 6. Observed urban areas : optical image (a), temporal mean of the corresponding SAR image (b), and the 3-D model from IGN and Google Earth used as a ground truth. The red line in (b) and white one in (c) correspond to the slice shown in Fig. 8

(a)

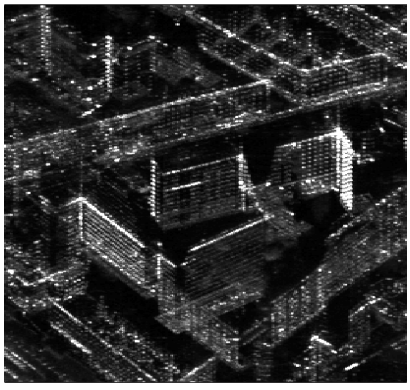

(b)

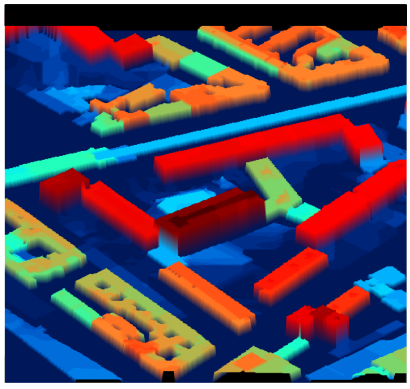

(c)

Fig. 7. Observed urban areas : optical image (a), temporal mean of the corresponding SAR image (b), and the 3-D model from IGN and Google Earth used as a ground truth.

The results are shown in Fig. 8 for the reconstructions of the slice, and in Fig. 10 and Fig. 11 for the reconstruction of the whole scenes. With the first experiment the behavior of each estimator and the resulting surface can be observed in greater details. In the reconstructions, the areas where the surface is occluding itself are detected as shadow areas and removed. The resulting gaps introduced are filled according to the height of the first point outside it.

A second experiment presents the evolution of the reconstructed slice as the REDRESS algorithm iterates *cf.*

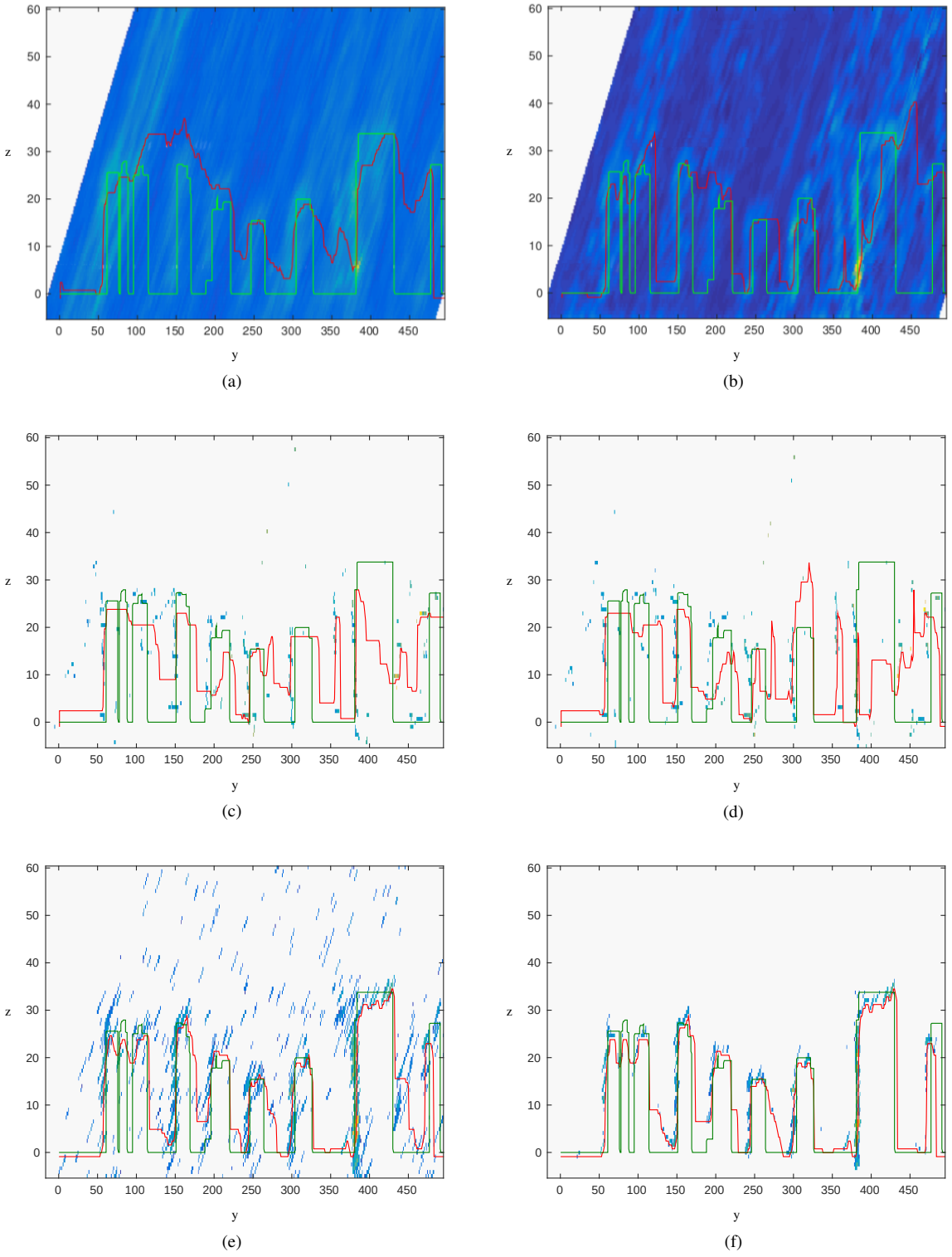

Fig. 8. Urban surface estimation using graph-cut segmentation of the tomograms, as described in section 3. The estimated surface corresponds to the red profile. The ground truth for the given slice is shown in green. The tomograms are obtained using Capon beamforming (a), SPICE (b), MUSIC (c), WSF (d), the 3-D inversion approach (e) and REDRESS (f).

Fig. 9. It can be observed that the distribution of reflectivities becomes much sharper after a few iterations.

The third experiment illustrates the role of the 3-D smoothing for both scenes. The surface is shown as seen from the sensor point of view. Since some tomographic estimators provide an estimate of the reflectivities, those reflectivities can be plotted to illustrate the distribution of scatterers on the reconstructed surfaces.

To estimate the covariance matrix at each point, we used a 7×7 Gaussian filter. For MUSIC and WSF, the number of scatterers is set constant and equal to 2 to avoid selecting too many outliers while allowing multiple scatterers within each radar resolution cell. For these two estimators, the reflectivity is estimated by mean square minimization, to keep a physical interpretation of the tomograms. As the scene is very heterogeneous with a lot of layover, this step introduces some undesired mixing of the information in the image. The surfaces estimated from tomographic reconstructions using spectral analysis techniques present noticeable artifacts in the dense areas. Some structures are too extended, partially filling streets or the building atrium. Meanwhile, the averaging step makes the tomographic estimation smoother in homogenous areas for the fully sparse approaches MUSIC and WSF.

The CS technique performed on all the data set presents results that seem visually the closest to the ground truth. Many details can be observed in this reconstruction: most of the rooftops and visible streets are well segmented and the buildings atrium are also retrieved.

For all the previous estimators, the TV minimization produces some building elongation resulting in phantom structure in low intensity signal area. This can be seen for instance in the bottom right part for Fig. 10 or around the position 450 for Fig. 8.

Finally, the reconstructions obtained using the REDRESS algorithm present the closest results to the ground truth with far less TV artifacts in dark areas. However, even with the alternated approach, some gaps between close and bright structures are filled in the reconstruction, as can be observed in the second scene. The information provided by the stack of SAR images does not seem sufficient to retrieve the ground height in this configuration. Including images with other incidence angles would help to estimate the heights in these locations.

To conduct a quantitative comparison of the segmentation results, we report the mean error for each estimated surface to the ground truth *cf.* 1. The TV parameter β is set, for each method, as the one minimizing this error.

Estimator	**Mean Error**		β
	Scene a	Scene b	
Capon Beamforming	4.58 m	5.84 m	1.5
MUSIC	3.23 m	4.00 m	1.3
WSF	3.12 m	4.00 m	1.6
SPICE	4.24 m	4.21 m	12.6
3-D inversion	2.50 m	2.60 m	2.0
REDRESS	**1.60 m**	**2.02 m**	2.0

Table 1. Mean errors between the estimated surfaces and the ground truth, last column: optimal β values used for the surface segmentation.

6. Conclusion

In this paper we introduced a graph-cut based segmentation algorithm to estimate the urban surfaces from a SAR tomographic reconstruction. The proposed approach is very general and can be used in combination with

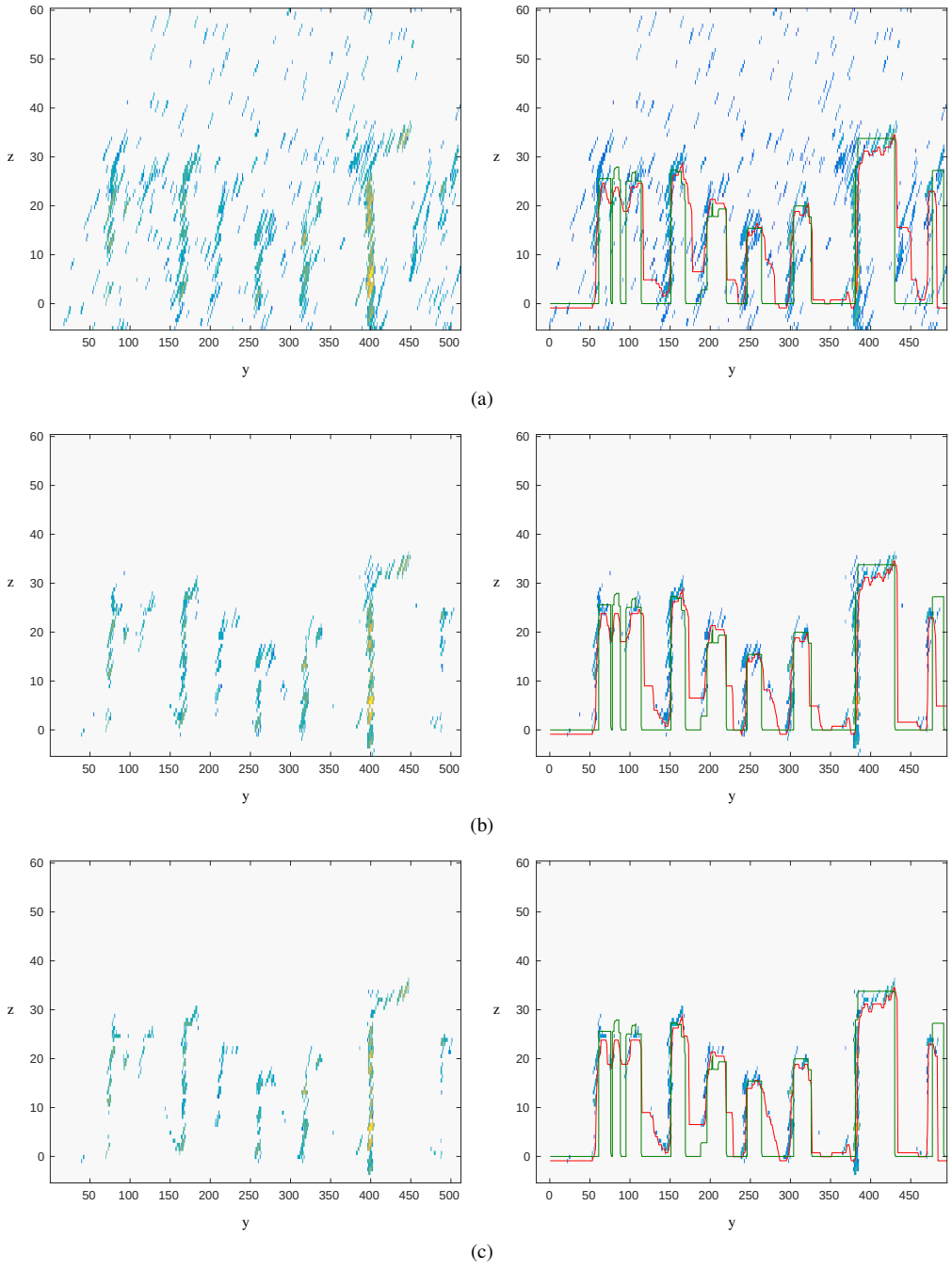

Fig. 9. Three different iteration steps from the alternate reconstruction algorithm. On the left column, the estimated reflectivities are shown for the profile presented in Fig 6. On the right, the estimated surface (red) and the ground truth (green) are superimposed in addition to the estimated reflectivities. Rows (a), (b) and (c) correspond respectively to the first, third and fifth iterations (last one).

many different tomographic algorithms. Experiments done on a set of 40 TerraSAR-X images of Paris show good results for different tomographic estimators (Capon beamforming, MUSIC, WSF, SPICE, CS and 3-D inversion). As the 3-D inversion algorithm is designed to use 3-D priors, we also present an algorithm that alternatively reconstructs the 3-D distribution of reflectivities, segments the urban surfaces from the volume of reflectivities and updates the regularization so as to improve the subsequent 3-D reconstruction. While the non-iterative 3-D

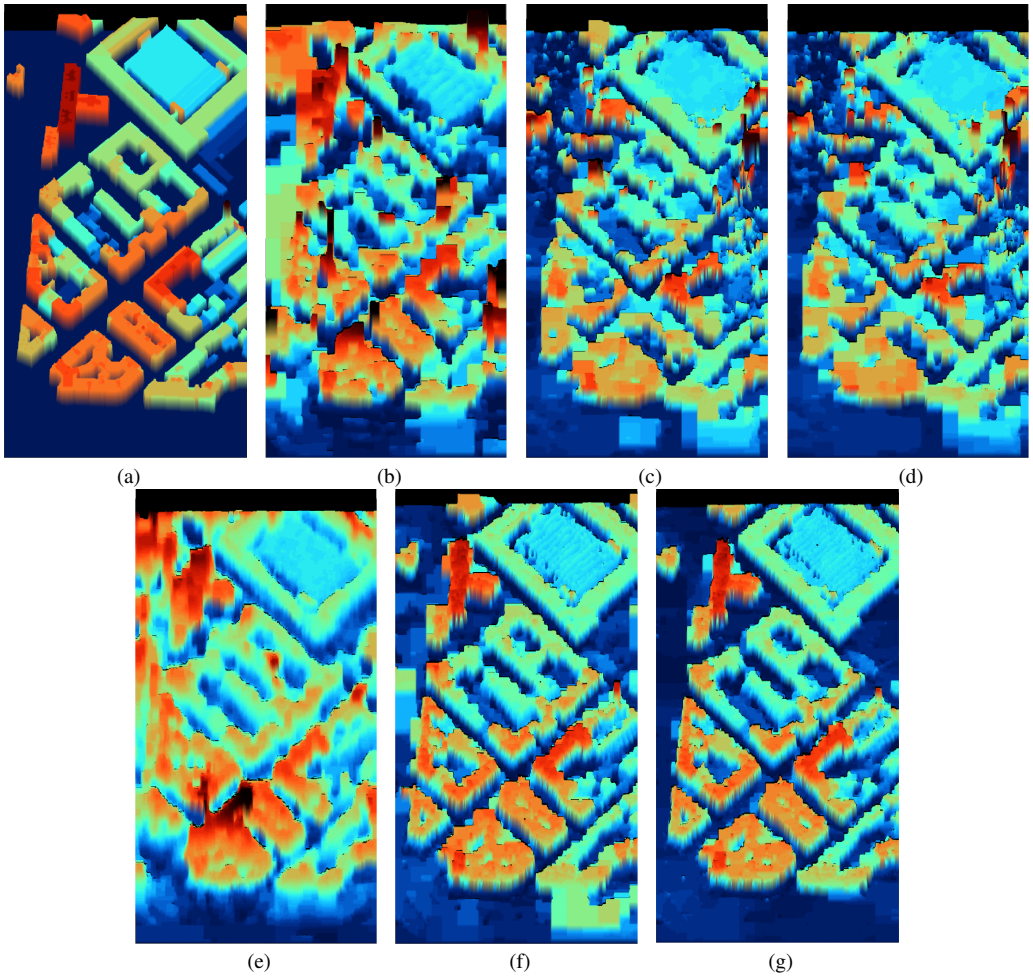

Fig. 10. Ground truth height (a), scene surface estimation using SPICE (b), MUSIC (c), WSF (d), Capon beamforming (e), the 3-D inversion (f) and REDRESS (g). For each results, the image shows the surface colored according to its height.

inversion algorithm fails in some cases to reduce the main lobes of the strong scatterers, the alternating scheme achieves a much sharper estimation of the distribution of reflectivities.

7. Acknowledgements

This project has been funded by ANR (the French National Research Agency) and DGA (Direction Générale de l'Armement) under ALYS project ANR-15-ASTR-0002.

The TerraSAR-X images were provided by the DLR in the framework of the project LAN1746.

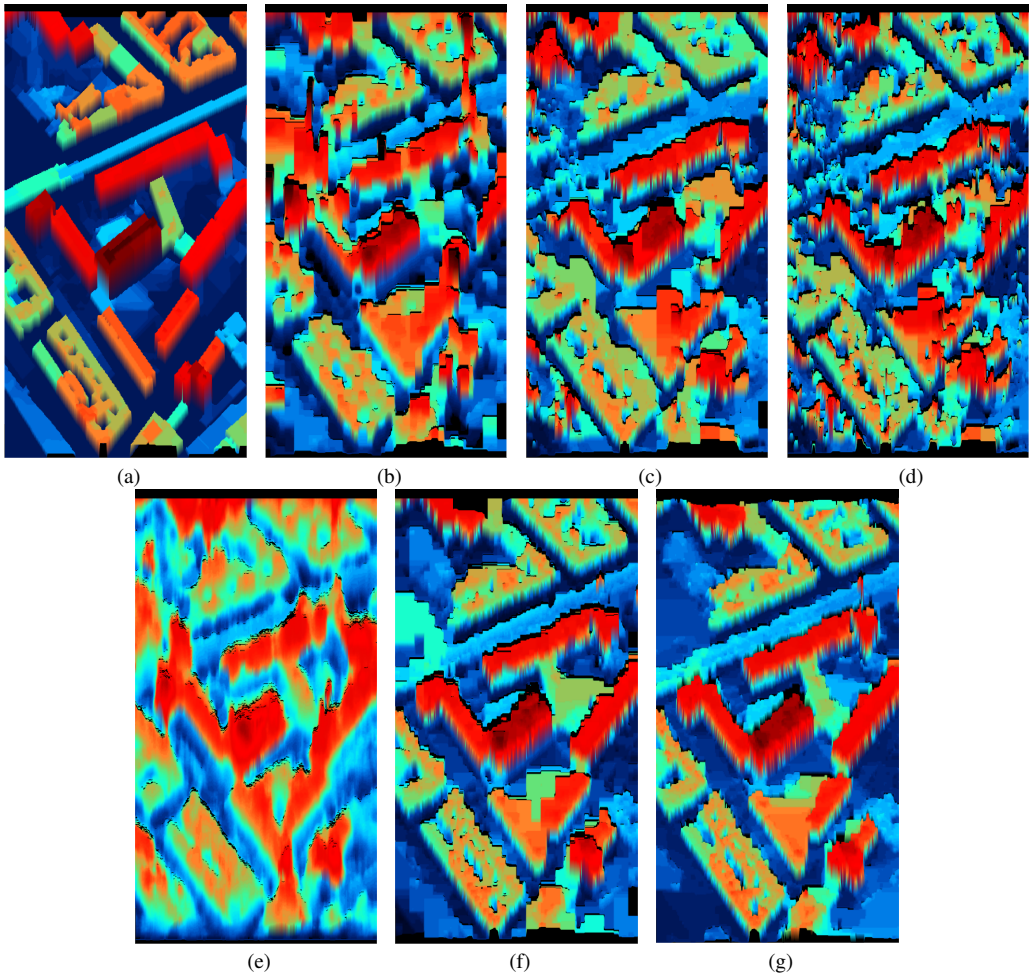

Fig. 11. Ground truth height (a), scene surface estimation using SPICE (b), MUSIC (c), WSF (d), Capon beamforming (e), the 3-D inversion (f) and REDRESS (g). For each results, the image shows the surface colored according to its height.

References

Boykov, Y., Kolmogorov, V., 2004. An experimental comparison of min-cut/max-flow algorithms for energy minimization in vision. IEEE transactions on pattern analysis and machine intelligence 26, 1124–1137.

Budillon, A., Evangelista, A., Schirinzi, G., 2011. Three-Dimensional SAR Focusing From Multipass Signals Using Compressive Sampling. IEEE Transactions on Geoscience and Remote Sensing 49, 488–499. doi:10.1109/TGRS.2010.2054099.

Capon, J., 1969. High-resolution frequency-wavenumber spectrum analysis. Proceedings of the IEEE 57(8), 1408–1418.

Fornaro, G., Serafino, F., Soldovieri, F., 2003. Three-dimensional focusing with multipass SAR data. IEEE Transactions on Geoscience and Remote Sensing 41, 507–517. doi:10.1109/TGRS.2003.809934.

Huang, Y., Ferro-Famil, L., Reigber, A., 2010. Under foliage object imaging using SAR tomography and polarimetric spectral estimators, in: 8th European Conference on Synthetic Aperture Radar, pp. 1–4.

Ishikawa, H., 2003. Exact optimization for Markov random fields with convex priors. IEEE Transactions on Pattern Analysis and Machine Intelligence 25, 1333–1336. doi:10.1109/TPAMI.2003.1233908.

Ley, A., D'Hondt, O., Hellwich, O., 2018. Regularization and Completion of TomoSAR Point Clouds in a Projected Height Map Domain , 1–11.

Lobry, S., Denis, L., Tupin, F., 2016. Multitemporal SAR Image Decomposition into Strong Scatterers, Background, and Speckle. IEEE Journal of Selected Topics in Applied Earth Observations and Remote Sensing 9, 3419–3429. doi:10.1109/JSTARS.2016.2555579.

P. Stoica, R.M., 1997. in: Introduction to Spectral Analysis, Prentice Hall.

Rambour, C., Denis, L., Tupin, F., Nicolas, J.M., Oriot, H., 2018. SAR Tomography Of Urban Areas: 3D Regularized Inversion In The Scene Geometry, in: 2018 IEEE International Geoscience and Remote Sensing Symposium (IGARSS).

Reigber, A., Moreira, A., 2000. First demonstration of airborne SAR tomography using multibaseline L-band data. IEEE Transactions on Geoscience and Remote Sensing 38, 2142–2152. doi:10.1109/36.868873.

Schmidt, R., 1986. Multiple emitter location and signal parameter estimation. IEEE Transactions on Antennas and Propagation 34, 276–280. doi:10.1109/TAP.1986.1143830.

Shahzad, M., Zhu, X.X., 2016. Automatic Detection and Reconstruction of 2-D/3-D Building Shapes From Spaceborne TomoSAR Point Clouds. IEEE Transactions on Geoscience and Remote Sensing 54, 1292–1310. doi:10.1109/TGRS.2015.2477429.

Stoica, P., Babu, P., Li, J., 2011. Spice: A sparse covariance-based estimation method for array processing. IEEE Transactions on Signal Processing 59, 629–638. doi:10.1109/TSP.2010.2090525.

Viberg, M., Ottersten, B., Kailath, T., 1991. Detection and estimation in sensor arrays using weighted subspace fitting. IEEE Transactions on Signal Processing 39, 2436–2449. doi:10.1109/78.97999.

Zhu, X.X., Bamler, R., 2010. Tomographic SAR Inversion by L_1 -Norm Regularization ; The Compressive Sensing Approach. IEEE Transactions on Geoscience and Remote Sensing 48, 3839–3846. doi:10.1109/TGRS.2010.2048117.

Zhu, X.X., Bamler, R., 2012. Super-Resolution Power and Robustness of Compressive Sensing for Spectral Estimation With Application to Spaceborne Tomographic SAR. IEEE Transactions on Geoscience and Remote Sensing 50, 247–258. doi:10.1109/TGRS.2011.2160183.

Zhu, X.X., Shahzad, M., 2014. Facade Reconstruction Using Multiview Spaceborne TomoSAR Point Clouds. IEEE Transactions on Geoscience and Remote Sensing 52, 3541–3552. doi:10.1109/TGRS.2013.2273619.